

New simulations of accreting DA white dwarfs: inferring accretion rates from the surface contamination

F. C. Wachlin¹, G. Vauclair^{2,3}, S. Vauclair^{2,3}, and L. G. Althaus¹

¹ Instituto de Astrofísica de La Plata (UNLP - CONICET). Facultad de Ciencias Astronómicas y Geofísicas. Universidad Nacional de La Plata, Argentina

e-mail: fcw@fcaglp.unlp.edu.ar

² Université de Toulouse, UPS-OMP, IRAP, France

³ CNRS, IRAP, 14 avenue Edouard Belin, 31400 Toulouse, France

September 24, 2021

ABSTRACT

Context. A non negligible fraction of white dwarf stars show the presence of heavy elements in their atmospheres. The most accepted explanation for this contamination is the accretion of material coming from tidally disrupted planetesimals, which form a debris disk around the star.

Aims. We provide a grid of models for hydrogen rich white dwarfs accreting heavy material. We sweep a 3D parameter space involving different effective temperatures, envelope's hydrogen content and accretion rates. The grid is appropriate for determining accretion rates in white dwarfs showing the presence of heavy elements.

Methods. Full evolutionary calculations of accreting white dwarfs were computed including all relevant physical processes, particularly the fingering (thermohaline) convection, a process neglected in most previous works, that has to be considered to obtain realistic estimations. Accretion is treated as a continuous process and bulk Earth composition is assumed for the accreted material.

Results. We obtain final (stationary or near stationary) and reliable abundances for a grid of models representing hydrogen rich white dwarfs of different effective temperatures and hydrogen contents, submitted to various accretion rates.

Conclusions. Our results provide realistic estimates of accretion rates to be used for further studies on evolved planetary systems.

Key words. (stars:) white dwarfs - stars: evolution - stars: abundances - stars: interiors - accretion, accretion disks - instabilities

1. Introduction

All the stars with masses lower than $8 M_{\odot}$, which constitute about 97% of the stellar population of the Galaxy, will end their evolution as white dwarfs. A large fraction of these stars host planets. The fate of these planetary systems, when the stars evolve from the main-sequence up to the final white dwarf stage, has been the subject of considerable interest during the last decades.

The infrared excess discovered around the DA white dwarf G29-38 (Zuckerman & Becklin 1987) and the photospheric contamination of white dwarfs by heavy elements are interpreted as the result of the disruption by tidal effects of planetesimals orbiting the white dwarf (Jura 2003). This scenario is confirmed by the observations of debris transiting the white dwarf WD1145+017 (Vanderburg et al. 2015) and the spectroscopic detection of planetesimal orbiting in the gaseous disk of SDSS1228+1040 (Manser et al. 2019). These observations show that small bodies in the planetary systems have survived during the host-star evolution. This implies that some planets must have survived as well. Such massive bodies are needed to perturbate the orbits of the planetesimals and push them inside the white dwarf tidal radius where they are disintegrated, as predicted by most scenarios of planetary systems evolution (Debes & Sigurdsson 2002; Debes et al. 2012; Mustill et al. 2013; Veras et al. 2013, 2014a,b, 2015a,b,c, 2016; Veras 2016; Frewen & Hansen 2014).

The disrupted planetesimals feed the debris disk, and part of it is accreted onto the white dwarf, thereby polluting its atmosphere. Since the diffusion time-scale of the accreted heavy elements through the white dwarf external layers is much shorter than the evolutionary time-scale, the presence of heavy elements in the photosphere implies that the accretion process is going-on. The study of the polluted white dwarfs is accordingly a powerful way to study the chemical composition of the planetesimals and to better understand the various physical processes at work in the evolution of the planetary systems.

The estimate of the accretion rates is an important input in this study. Most previous estimates of accretion rates were obtained by assuming that the accreted material, completely mixed in the surface convection zone, diffuses downwards on a diffusion time scale (Farihi et al. 2012; Koester et al. 2014). Recently, Cunningham et al. (2019) explored the macroscopic diffusion induced by convective overshoot in DA white dwarfs by using three-dimensional (3D) simulations with the CO5BOLD code. Such an increase of the mixed zone leads to larger accretion rates.

Deal et al. (2013); Wachlin et al. (2017) and Bauer & Bildsten (2018, 2019) introduced in their computations the fingering convection process, which is indeed unavoidable in this context, since the accreted material, with a chemical composition mostly similar to that of the solar system bodies (Swan et al. 2019) has a mean molecular weight larger than that of the white dwarf atmospheres. The inverse μ -gradient

produces a double-diffusive instability, inducing extra-mixing of the accreted material (see for example Vauclair (2004); Stancliffe et al. (2007); Garaud (2011); Wachlin et al. (2011); Brown et al. (2013); Wachlin et al. (2014); Zemska et al. (2014)).

As shown by Deal et al. (2013) and confirmed by Wachlin et al. (2017) and Bauer & Bildsten (2018, 2019), this fingering convection has important consequences in the case of accreting DA white dwarfs, whereas it is absent or marginal in DB white dwarfs. In DA white dwarfs, the accretion rates needed to reproduce the photospheric abundances of heavy elements exceed by up to 2 orders of magnitude those estimated without this effect.

In this paper, we present the results of a series of numerical simulations of accretion onto DA white dwarfs. Our aim is to provide estimates of the accretion rates and of the photospheric chemical composition for a choice of heavy elements among the most often observed in polluted white dwarfs. Our simulations cover a large range of parameters for the effective temperature, hydrogen mass fraction and accretion rates. From these results, it is possible to infer an estimate of the accretion rate needed to reproduce the heavy element abundances deduced from the observations, knowing the effective temperature of the white dwarf. In section 2 we define the range of parameters covered by the simulations and describe how we obtain the initial models. Section 3 describes how the simulations have been performed. Section 4 gives the results of our simulations. A summary and a discussion of these results are given in section 5.

2. Initial models

To study the relation between the accretion rate and the resulting surface contamination of hydrogen-rich (DA) white dwarfs, we prepared a set of numerical experiments involving models of white dwarfs with different effective temperatures and different amounts of hydrogen content in their envelopes, (M_H). In particular, we choose the following effective temperatures: 6000K, 8000K, 10000K, 10500K, 11000K, 11500K, 12000K, 16000K, 20000K and 25000K and the following M_H values: $10^{-4}M_\odot$, $10^{-6}M_\odot$, $10^{-8}M_\odot$ and $10^{-10}M_\odot$. The value of M_H is particularly relevant since it impacts the depth of the transition zone between hydrogen-rich and helium-rich layers.

All initial setups are based on the $0.609 M_\odot$ ($Z = 0.01$) white dwarf model obtained by Renedo et al. (2010) from the full evolution of its progenitor star from the zero-age main sequence (ZAMS) to advanced stages on the thermally-pulsing asymptotic giant branch. To generate white dwarf configurations with smaller hydrogen contents than that dictated by progenitor evolution, we artificially reduced the hydrogen content by converting the excess of hydrogen into helium. This is enough for our purposes. In this work, we considered for each model four different accretion rates, namely $\log(\dot{M}) = 6, 8, 10, 12$, where \dot{M} is given in g.s^{-1} .

3. Numerical simulations

The white dwarf models used in this work were generated by the LPCODE stellar evolution code. This code has been tested and widely used in various stellar evolution contexts of low-mass and white dwarf stars (see Althaus et al. 2003, 2005;

Salaris et al. 2013; Althaus et al. 2015; Miller Bertolami 2016; Silva Aguirre et al. 2020; Christensen-Dalsgaard et al. 2020, for details). An interesting point for the present work is that LPCODE computes the white dwarf evolution in a self-consistent way, including the modifications in the internal chemical distribution induced by dynamical convection, fingering convection, atomic diffusion, and nuclear reactions. Atomic diffusion has been implemented following Burger's scheme (Burgers 1969) that provides the diffusion velocities in a multicomponent plasma under the influence of gravity, partial pressure, and induced electric fields. Partial ionization of metals is taken into account as it has important effects for the diffusion timescales.

We have introduced some changes in the code in order to simulate the accretion process. All computations were done by considering accretion as a continuous process. Accreted material was assumed to be uniformly distributed on the star's surface (see below). We performed simulations for different accretion rates, ranging from 10^6 g/s to 10^{12} g/s . Metal abundances of accreted matter were set to mimic the composition of the bulk Earth (Allègre et al. 2001). Finally we used OPAL radiative opacities for different metallicities (Iglesias & Rogers 1996), complemented with the molecular opacities from (Alexander & Ferguson 1994) at low temperatures. Since bulk Earth composition was adopted for the accreted matter, a new set of opacity tables was generated from the OPAL website following this composition.

Considering that DA white dwarfs develop a convective envelope at effective temperatures lower than about 15000 K, we implemented the accretion process in two different ways, depending on the presence or not of envelope convection. For those models with a convective envelope, the accreted material was instantaneously mixed in that region. This is a reasonable approximation since the convection timescale is much shorter than the evolutionary timescale. Specifically, for a given integration timestep, we estimate the amount of material that is accreted according to the accretion rate, and this material is uniformly distributed in the whole convective zone. At higher effective temperatures, when convection is absent, a different criterion is instead required to distribute the accreted material in the very outer layers of the star. In this case, different approaches have been used in the past, either based on some arbitrary selection of the depth at which the accreted matter should be distributed homogeneously (Koester & Wilken 2006; Koester 2009) or by considerations that neglect the role of fingering convection instability (Gänsicke et al. 2012). It is worth noting that the deepening of the fingering convection instability eventually makes the choice of that depth less critical. We performed additional calculations to verify this.

In this work, particular attention has been paid to the evolution of ^{16}O , ^{24}Mg , ^{28}Si , ^{40}Ca and ^{56}Fe . These elements are important since they have been detected in the photospheres of many white dwarfs. Their presence in the final surface composition of our simulations allow us to link any given accretion rate with these surface abundances for each model, characterized by its effective temperature and amount of hydrogen.

The computation of energy transport was performed by using the double diffusion theory of Grossman et al. (1993) as described by Wachlin et al. (2011) Diffusion coefficients for fingering convection zones were obtained by adopting the prescription of Brown et al. (2013).

Table 1. Adopted values for the set of parameters characterizing each model.

parameter	adopted values
$\log(M_{\text{H}}/M_{\odot})$	-4, -6, -8, -10
$\log \dot{M}$	6, 8, 10, 12 ^a
$T_{\text{eff}}/10^3\text{K}$	6 ^b , 8 ^c , 10, 10.5, 11, 11.5, 12, 16, 20, 25

Notes. Some combinations of parameters have been discarded because of the following reasons:

(^a) For maximum accretion rate, models with $\log(M_{\text{H}}/M_{\odot}) = -10$ and $T_{\text{eff}} \geq 10000\text{K}$ run out of our opacity tables because of the excess of metal accumulation at the surface.

(^b) Transforms into a DB white dwarf for $\log(M_{\text{H}}/M_{\odot}) = -8$ and -10 .

(^c) Same as (b) but for $\log(M_{\text{H}}/M_{\odot}) = -10$ models.

4. Results

In this section we describe the main results of our simulations, paying special attention not only to the final composition of the atmosphere but to the whole process that leads to the final state. Our models are characterized by three main parameters:

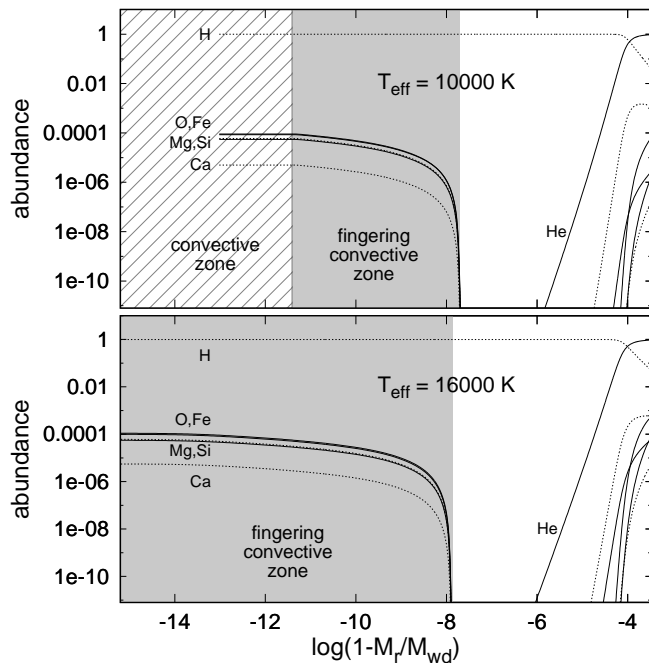
1. the amount of hydrogen contained in the envelope (M_{H}),
2. the effective temperature (T_{eff}),
3. the accretion rate (\dot{M}).

As mentioned before, four different models were considered, based on the amount of hydrogen that remains from the previous evolution. For each model we took initial configurations with ten different effective temperatures, ranging from 6000 K to 25000 K. Finally we submitted each model to four different accretion rates. The total number of simulations performed was 180. Table 1 shows the details of the parameters adopted for each set of models. Some sets of parameters could not be combined to perform the corresponding simulation because either the initial model was impossible to be generated as a hydrogen rich (DA) white dwarf, or because a thin hydrogen envelope combined with a large accretion rate produced surface compositions running out of the opacity tables.

According to its effective temperature, a model may present a convective envelope or not. This fact has some impact on the internal structure once a stationary state is reached. For instance, Fig. 1 shows the final chemical profile for two models with the largest amount of hydrogen ($10^{-4}M_{\odot}$), one having a convective envelope while the other not. Both models were obtained from an accretion rate of 10^{10} g/s . Convection mixes up the composition of the superficial layers in a very short timescale, thus leading to a homogeneous abundance of all elements in that region (shown in the figure as a horizontal line in the convective zone, CZ hereafter). Below the convective region and because of the inversion of the molecular weight (μ), a fingering convective zone (FCZ) sets in. As we will discuss later, the turbulent motions generated by this instability right below the bottom of the convective zone is responsible for transporting the heavy elements coming from the upper layers down into the deeper regions of the star. This figure clearly shows how the turbulence in the FCZ diminishes as we go deeper. Indeed, the slope of the chemical profile of the heavy elements in that region goes from almost horizontal (more homogeneously distributed material) near the bottom of the CZ, to very steep at the bottom of the FCZ, characterized by a smooth transition to the radiative transport regime. It is worth mentioning that since fingering convection is a more efficient process than element diffusion, larger accretion rates are needed

Table 2. Final iron surface abundances (in mass) for simulations turning on and off fingering convection. Three accretion rates were considered for initial models all having the same amount of hydrogen ($M_{\text{H}} = 10^{-4}M_{\odot}$) and effective temperature ($T_{\text{eff}} = 10000\text{ K}$).

	10^6 g/s	10^8 g/s	10^{10} g/s
including FC	0.80×10^{-7}	0.35×10^{-5}	0.90×10^{-4}
without FC	0.27×10^{-6}	0.27×10^{-4}	0.27×10^{-2}


Fig. 1. Final chemical profile for two models with $M_{\text{H}} = 10^{-4}M_{\odot}$ but different effective temperatures. The accretion rate in both cases was of 10^{10} g s^{-1} .

to maintain a given surface contamination when fingering convection is taken into account, as shown by Deal et al. (2013) and Wachlin et al. (2017). We may show the incidence of taking fingering convection into account by comparing the final (stationary) surface abundance of one representative metal, namely iron, for simulations where we have turned on and off this process. Table 2 shows the results for these simulations performed using the same base model which has $M_{\text{H}} = 10^{-4}M_{\odot}$ and $T_{\text{eff}} = 10000\text{ K}$. From the table it becomes clear that fingering convection needs to be included when associating a surface contamination with the corresponding accretion rate.

Fig. 2 displays the temporal evolution of the photosphere's abundance of iron for an accretion rate of 10^6 g s^{-1} at three different effective temperatures. We note that for the hotter models, those with $T_{\text{eff}} = 8000\text{ K}$ and 10000 K , the abundance of iron reaches a stationary state well before the end of the simulation, which was set after 14000 yr of continuous accretion. However, at the lowest effective temperature, much more time is required to reach the stationary state (about 200000 yr). This is an expected behavior since as CZ becomes more massive as cooling proceeds, more time is needed to achieve the final (stationary) state. We mention that all of our simulations have been extended in order to reach a final state as close as possible to a stationary situation.

Fig. 3 reveals another feature of our simulations, namely, the contrast between the time required for the surface heavy ele-

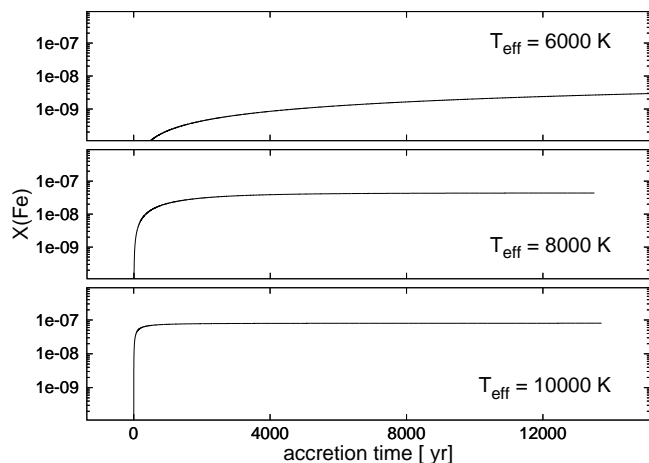


Fig. 2. Temporal evolution of the abundance (in mass) of iron for a continuous accretion rate of 10^6 g s^{-1} for white dwarf models with a hydrogen content of $10^{-4} M_{\odot}$ at three selected effective temperatures.

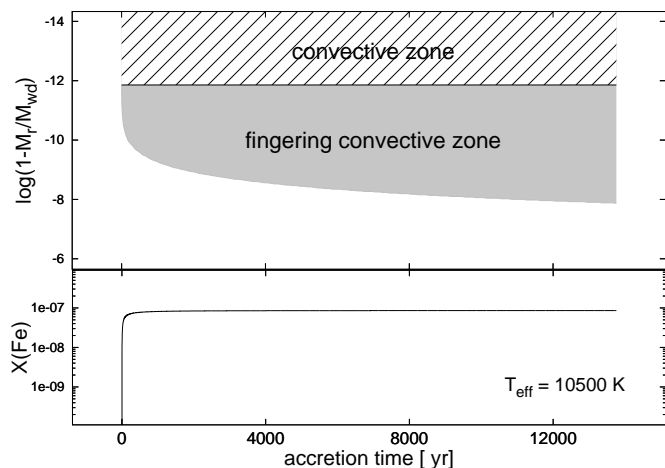


Fig. 3. Upper panel: time evolution of the convective and fingering convective zone during the accretion period for a model with $T_{\text{eff}} = 10500 \text{ K}$, $M_{\text{H}} = 10^{-4} M_{\odot}$ and accretion rate of 10^6 g s^{-1} . Bottom panel: evolution of the iron abundance (in mass) at the surface.

ments to reach the stationary state and the evolution of the FCZ. Indeed, while the abundance of iron, as well as that of the other heavy elements accreted (not shown), rapidly reach a stationary state, the bottom of the FCZ continues moving to deeper layers during white dwarf evolution. This is in contrast with the situation shown in Fig. 4 for the case of a smaller H envelope. Here, the inward advance of the bottom of the FCZ is halted by the H-He transition, where the inverse μ -gradient produced by the accretion is counteracted by the strong chemical gradient at the H-He interface. We note that in this case the evolution of the iron abundance is the same as that shown in Fig. 3, i.e. the stationary state is reached in a short time.

The impact of a thinner FCZ on the accumulation of heavy elements on the surface increases when the H-He transition is closer to the photosphere of the star. Fig. 5 illustrates how thin the FCZ becomes when the hydrogen mass in the envelope is reduced to $10^{-10} M_{\odot}$. In this case the bottom of the CZ penetrates more in the He-rich layers, lowering the contrast between the molecular weights inside the CZ and below. Because of the effect of the stabilizing μ -gradient produced by the increasing helium abundance as we go deeper, fingering convection barely shows

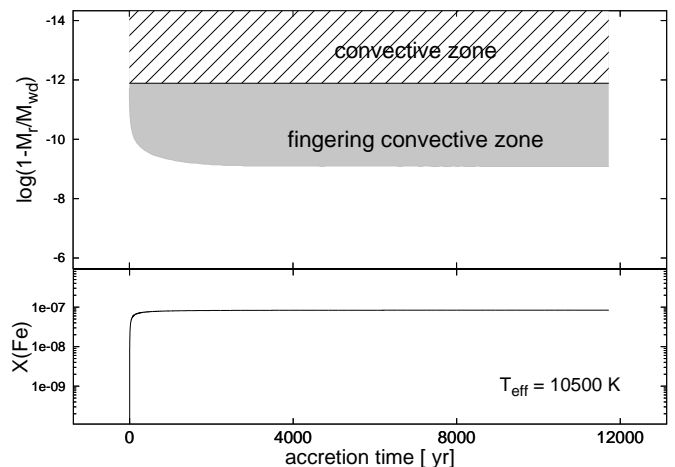


Fig. 4. Same as Fig. 3 but for a model with $M_{\text{H}} = 10^{-6} M_{\odot}$.

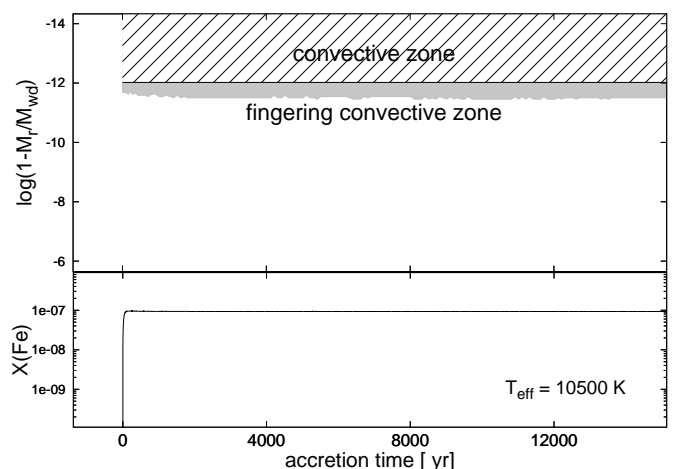


Fig. 5. Same as Figure 3 but for a model with $M_{\text{H}} = 10^{-10} M_{\odot}$.

up. The extension of the FCZ also depends on the accretion rate: the higher the accretion rate the wider the FCZ (not shown in the figure). In the case shown in Fig. 5, the abundance of iron increases by 15% with respect to the cases with a larger hydrogen envelope. Other simulations show a much higher accumulation of heavy elements when the FCZ becomes thin.

Models with a larger content of hydrogen have the H-He transition deeper and that may cause this region to be unreachable for the FCZ. In fact, all our simulations using models with $M_{\text{H}} = 10^{-4} M_{\odot}$ show that the bottom of the FCZ does not reach the H-He transition layers. Thus, the FCZ finds no obstacle to advance deeper as the simulation continues, although it slows down its pace as it penetrates into layers of increasing density. In contrast, the bottom of the convective zone (when the model has one) remains always at the same depth. Since the extension of the convective zone depends on the effective temperature, the level of accumulation of heavy elements on the surface will also depend on this parameter. Cooler models, with larger convective zones, rapidly spread the accreted material into this larger region, producing a lower contamination of the surface than in hotter white dwarfs. The evolution of the FCZ is faster for higher accretion rates, it also goes deeper carrying the heavy material further inside the star.

Figure 6 shows the chemical profile at the end of the simulation for a model with $M_{\text{H}} = 10^{-4} M_{\odot}$, $T_{\text{eff}} = 10000 \text{ K}$ and

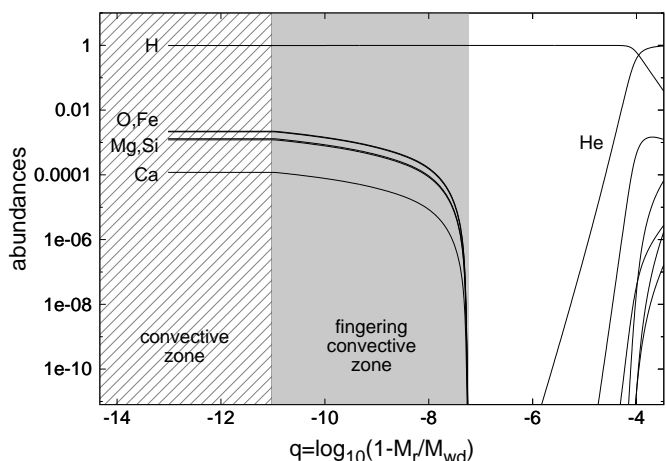


Fig. 6. Chemical profile of the final configuration of a model with $10^{-4}M_{\odot}$ of hydrogen, $T_{\text{eff}} = 10000$ K and accretion rate of 10^{12} g s $^{-1}$.

maximum accretion rate (10^{12} g s $^{-1}$). The FCZ embraces a large region of the star (in a logarithmic scale in mass) but is still far from reaching the He-rich layers. Accreted heavy elements are homogeneously distributed along the convective zone but are less and less abundant as we advance deeper through the FCZ. The turbulence associated to the fingering convective instability is maximum near the bottom of the convective zone and diminishes gradually in the direction to the interior. Although there is a sharp step in turbulence in the frontier between convective and fingering convective zones, the transition from the bottom of the FCZ to the radiative regime is very smooth, with the turbulence gradually tending to zero. As stated before, the advance of the FCZ is faster for higher accretion rates. In particular, for the case of our maximum accretion rate shown in Fig. 6, it takes about 270 yr for the bottom of the FCZ to reach the layer $q = -7.63$, as compared with 14000 yr that is needed in the case that the accretion rate is 10^6 g s $^{-1}$.

In the case of thinner envelopes, the chemical evolution of accreting white dwarfs is quite different from the $M_{\text{H}} = 10^{-4}M_{\odot}$ case described before. The main reason for such a difference is that now the turbulence from the upper layers is able to reach the H-He transition zone, something that does not happen for thicker envelopes.

We may start by describing our results for models with $M_{\text{H}} = 10^{-6}M_{\odot}$. For such a thin envelope, the FCZ which develops below the CZ expands until penetrating the transition zone where He becomes more abundant¹. This encounter prevents the FCZ to go deeper, as it is stabilized by the normal μ -gradient due to the increasing amount of He. Thus, the heavy elements accumulated in the FCZ continue to progress further down by diffusion in a radiative medium, something that never happened in our previously described simulations of models with thicker envelopes, since the presence of heavy elements in a H-rich medium always triggered the fingering convection instability.

¹ We found only two cases where no FCZ was formed. Both simulations correspond to the coolest models ($T_{\text{eff}} = 6000$ K) and to the lower accretion rates (10^6 and 10^8 g s $^{-1}$). Two related facts are responsible for this result. First, the bottom of the convective zone deeply penetrates the H-He transition region reaching a stabilizing μ -gradient due to the increasing abundance of He as we go deeper. Second, the low accretion rate combined with a large CZ (which strongly dilutes the abundance of heavy elements), lowers the contrast of molecular weights at each side of the bottom of the CZ. The combination of these factors precludes the formation of the FCZ.

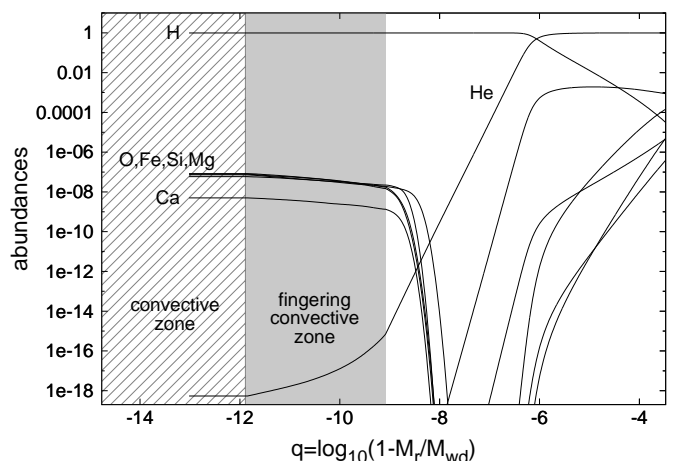


Fig. 7. Chemical profile of the final configuration of a model with $10^{-6}M_{\odot}$ of hydrogen, $T_{\text{eff}} = 10500$ K and accretion rate of 10^6 g s $^{-1}$.

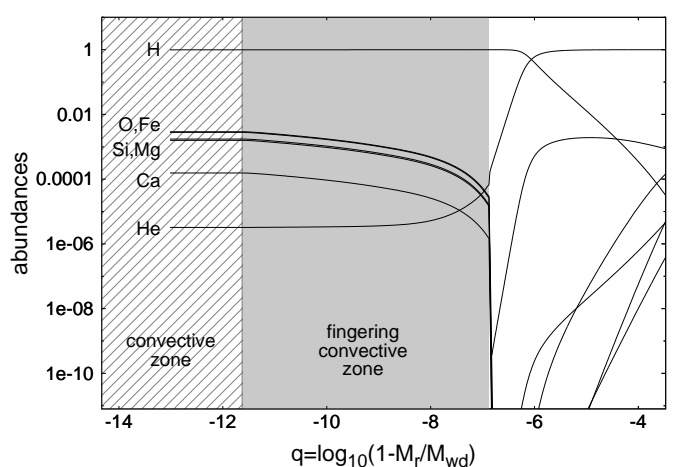


Fig. 8. Same as Fig. 7 but for a model with $10^{-6}M_{\odot}$ of hydrogen, $T_{\text{eff}} = 10500$ K but accretion rate of 10^{12} g s $^{-1}$.

ity. Figure 7 shows such a situation for a model of $T_{\text{eff}} = 10500$ K and an accretion rate of 10^6 g s $^{-1}$. We expanded the abundance range to include very low values in order to show the contact between the bottom of the FCZ and the He tail, which stops the instability. We also note the dredge-up of He by the FCZ, which leads to the contamination of the surface by a very small amount in this case.

Larger He contamination is expected in the case of larger accretion rates, see Fig. 8. In this case, the FCZ is able to further penetrate the H-He transition region, with the consequent larger He enrichment of the outer layers. All the simulations with the highest accretion rates show this kind of behavior. Unfortunately the abundance of He on the surface takes much longer to reach a steady state than the accreted heavy elements, and we had to stop the simulations before that state was reached. Thus, our tabulated abundances of helium are only lower boundaries in most cases.

Models with $M_{\text{H}} = 10^{-8}M_{\odot}$ share many of the main features of the $M_{\text{H}} = 10^{-6}M_{\odot}$ case. Dredge-up of helium is much more efficient now and consequently the contamination of the surface by helium is noticeably higher. The thinnest envelope models ($M_{\text{H}} = 10^{-10}M_{\odot}$) continues with the same tendency: more helium contamination of the surface and a FCZ advance stopped earlier by the more superficial H-He transition zone.

Figures 9 to 12 show how the surface contamination changes with the accretion rate for models of four different hydrogen envelopes. The details of the abundances at the end of each simulation are summarized in Tables 3 to 5.

5. Summary and Discussion

We have presented a series of numerical simulations concerning the accretion of material produced by the disintegration of small rocky bodies onto DA white dwarfs. These simulations consider the effect of the double-diffusive instability, referred to as fingering convection. This instability is induced by the inverse μ -gradient resulting from the accretion of heavy material on the white dwarf outer layers. Our simulations aimed at providing realistic estimates of the accretion rates, deduced from the observed heavy elements abundances in WD atmospheres, for a large range of effective temperatures, hydrogen-mass fractions and accretion rates. The results are presented in various graphs and tables, in such a way that the accretion rate may easily be deduced from the values of the heavy elements abundances. When fingering convection is properly considered, the resulting accretion rates may be up to several orders of magnitude larger than those estimated when ignoring its effect. For given values of the accretion rate and effective temperature, the accumulation of heavy elements in the WD atmospheres increases for decreasing hydrogen mass-fraction, since the fingering convection zone becomes thinner when the H/He transition zone is closer to the surface. In the cases of thin hydrogen mass-fraction and high accretion rates, the fingering convection may dredge-up some fraction of He from the H/He transition zone (see Tables 4 and 5). Such an effect produces DABZ type white dwarfs. We discuss below the various assumptions that have been adopted in our simulations. The chemical composition of the accreted material is supposed to be similar to the Earth bulk composition. This is the case for most observed polluted DA white dwarfs (Swan et al. 2019). There are also evidences of other white dwarfs polluted by material with a variety of chemical composition (Gänsicke et al. 2012; Wilson et al. 2015; Melis & Dufour 2017) including water-rich and hydrated planetesimals (Farihi et al. 2013; Raddi et al. 2015; Hoskin et al. 2020) and volatile-rich planetesimals (Xu et al. 2017). Our simulations are not representative of such cases.

The accreted material is supposed to be mixed through the convection zone and through the fingering convection zone. Cunningham et al. (2021) find from their 3-D radiation-hydrodynamics simulations that DA white dwarfs with effective temperature larger than 13000 K are unable to spread the accreted material horizontally on a time scale shorter than the diffusion time scale. However these diffusion time scales, estimated at the bottom of the convection zone, do not take into account the additional fingering convection zone. By considering fingering convection, diffusion happens deeper in the star and in a time scale which might be significantly longer. The fact that there is currently no detection of surface abundance variations in polluted DA white dwarfs (Debes & López-Morales 2008; Reach et al. 2009; Wilson et al. 2019) suggests that the horizontal mixing is more efficient than predicted. Thus our assumption of a horizontal mixing in turbulent zones seems realistic.

The simulations assume a constant accretion rate. In some case however, the disintegration of a planetesimal in small pieces could result in time variability of the accretion rate. This may be the case for instance for WD1145+017 (see Gänsicke et al. 2016; Rappaport et al. 2016; Redfield et al. 2017; Gary et al. 2017; Izquierdo et al. 2018, for details).

Table 3. Models with $M_H = 10^{-4} M_\odot$. Abundances are expressed in $[Z/H]$, where $[Z/H] = \log n(Z)/n(H)$ is the logarithmic number ratio of the abundance (in number) of element Z relative to the abundance of hydrogen (H). Lower values are marked by a > sign, when the stationary state was not achieved and the surface abundance of that element was still increasing.

		10^6 g s^{-1}	10^8 g s^{-1}	10^{10} g s^{-1}	10^{12} g s^{-1}
6000 K	He	-20.34	-19.67	-19.15	-19.25
	O	-9.16	-7.29	-5.88	-4.73
	Mg	-9.31	-7.62	-6.34	-5.16
	Si	-9.35	-7.66	-6.38	-5.21
	Ca	-10.63	-8.88	-7.56	-6.38
	Fe	-9.50	-7.76	-6.45	-5.30
8000 K	He	-29.63	-26.03	-25.35	-21.38
	O	-8.60	-6.86	-5.50	-3.99
	Mg	-8.83	-7.24	-5.92	-4.44
	Si	-8.91	-7.29	-5.95	-4.47
	Ca	-10.12	-8.49	-7.16	-5.67
	Fe	-9.11	-7.43	-6.07	-4.57
10000 K	He	-29.84	-25.00	-24.15	-21.93
	O	-8.34	-6.67	-5.28	-3.85
	Mg	-8.62	-7.02	-5.64	-4.29
	Si	-8.64	-7.05	-5.67	-4.33
	Ca	-9.91	-8.30	-6.90	-5.52
	Fe	-8.84	-7.21	-5.79	-4.41
10500 K	He	-29.61	-24.73	-23.87	-19.56
	O	-8.30	-6.65	-5.25	-3.74
	Mg	-8.60	-7.00	-5.61	-4.20
	Si	-8.58	-7.00	-5.62	-4.23
	Ca	-9.89	-8.28	-6.88	-5.42
	Fe	-8.81	-7.19	-5.76	-4.32
11000 K	He	-28.54	-24.79	-21.93	-23.69
	O	-8.12	-6.98	-5.18	-3.74
	Mg	-8.46	-7.03	-5.53	-4.21
	Si	-8.43	-6.96	-5.53	-4.24
	Ca	-9.72	-8.43	-6.81	-5.44
	Fe	-8.64	-7.27	-5.68	-4.33
11500 K	He	-27.43	-29.25	-27.12	-23.95
	O	-7.87	-6.44	-5.01	-3.62
	Mg	-8.21	-6.85	-5.48	-4.09
	Si	-8.18	-6.88	-5.51	-4.12
	Ca	-9.45	-8.10	-6.70	-5.31
	Fe	-8.37	-7.01	-5.60	-4.21
12000 K	He	-28.69	-29.32	-25.13	-24.59
	O	-9.18	-6.76	-4.97	-3.63
	Mg	-8.89	-6.91	-5.44	-4.09
	Si	-8.80	-6.92	-5.46	-4.12
	Ca	-10.51	-8.27	-6.66	-5.31
	Fe	-9.39	-7.19	-5.56	-4.20
16000 K	He	-27.03	-28.08	-23.90	-23.41
	O	-9.72	-7.12	-5.16	-3.81
	Mg	-9.43	-7.23	-5.63	-4.29
	Si	-9.21	-7.14	-5.66	-4.32
	Ca	-11.35	-8.77	-6.86	-5.50
	Fe	-10.19	-7.56	-5.75	-4.40
20000 K	He	-25.67	-26.95	-22.92	-22.45
	O	-9.76	-7.24	-5.33	-3.98
	Mg	-9.46	-7.36	-5.81	-4.46
	Si	-9.24	-7.28	-5.84	-4.49
	Ca	-11.39	-8.90	-7.03	-5.68
	Fe	-10.23	-7.68	-5.92	-4.57
25000 K	He	-22.46	-25.57	-21.90	-21.19
	O	-8.26	-7.37	-6.07	-4.16
	Mg	-8.66	-7.49	-6.21	-4.65
	Si	-8.69	-7.36	-6.10	-4.68
	Ca	-9.90	-9.03	-7.73	-5.86
	Fe	-8.81	-7.82	-6.52	-4.76

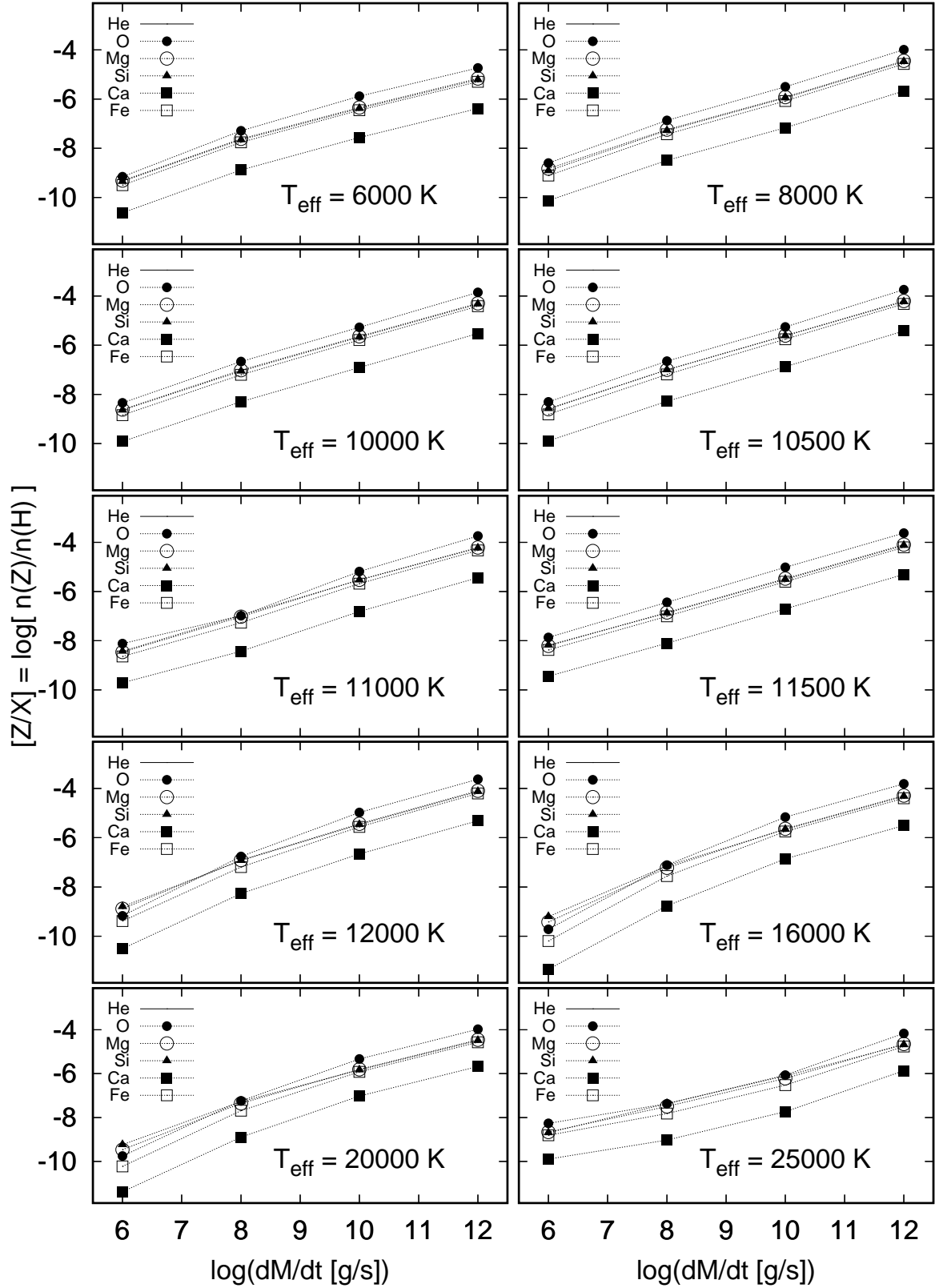


Fig. 9. Surface contamination against the accretion rate for models with $M_H = 10^{-4} M_\odot$. The contamination is given in terms of the abundance expressed in $[Z/H] = \log n(Z)/n(H)$.

Table 4. Same as Table 3 for models with $M_{\text{H}} = 10^{-6} M_{\odot}$
Table 5. Same as Table 3 for models with $M_{\text{H}} = 10^{-8} M_{\odot}$

	10^6 g s^{-1}	10^8 g s^{-1}	10^{10} g s^{-1}	10^{12} g s^{-1}		10^6 g s^{-1}	10^8 g s^{-1}	10^{10} g s^{-1}	10^{12} g s^{-1}		
6000 K	He	-8.50	-8.33	-7.87	> -7.74	8000 K	He	-8.65	-6.63	-4.81	> -2.70
	O	-9.34	-7.51	-6.37	-5.16		O	-8.62	-6.72	-5.45	-3.99
	Mg	-9.71	-7.94	-6.85	-5.65		Mg	-8.81	-7.03	-5.89	-4.44
	Si	-9.74	-7.97	-6.88	-5.68		Si	-8.92	-7.07	-5.92	-4.48
	Ca	-10.95	-9.15	-8.06	-6.86		Ca	-10.12	-8.30	-7.15	-5.68
	Fe	-9.83	-8.04	-6.96	-5.75		Fe	-9.10	-7.27	-6.04	-4.59
8000 K	He	-17.79	-14.07	-11.12	> -6.83	10000 K	He	-10.24	-6.81	-4.78	> -3.96
	O	-8.61	-6.85	-5.44	-3.92		O	-8.35	-6.60	-5.26	-3.92
	Mg	-8.83	-7.23	-5.83	-4.38		Mg	-8.62	-6.89	-5.64	-4.37
	Si	-8.91	-7.27	-5.87	-4.41		Si	-8.65	-6.93	-5.68	-4.40
	Ca	-10.13	-8.48	-7.09	-5.61		Ca	-9.91	-8.19	-6.91	-5.59
	Fe	-9.11	-7.42	-6.00	-4.51		Fe	-8.85	-7.12	-5.79	-4.49
10000 K	He	-18.86	-14.71	-12.18	> -6.20	10500 K	He	-10.27	-6.77	-4.77	> -2.60
	O	-8.34	-6.68	-5.27	-3.76		O	-8.32	-6.59	-5.25	-3.78
	Mg	-8.62	-7.04	-5.63	-4.21		Mg	-8.61	-6.89	-5.62	-4.23
	Si	-8.64	-7.07	-5.67	-4.25		Si	-8.60	-6.90	-5.64	-4.26
	Ca	-9.91	-8.31	-6.90	-5.44		Ca	-9.90	-8.19	-6.89	-5.46
	Fe	-8.84	-7.22	-5.79	-4.33		Fe	-8.83	-7.11	-5.77	-4.35
10500 K	He	-18.87	-14.64	-12.05	> -6.09	11000 K	He	-10.54	-6.82	-4.80	> -2.62
	O	-8.31	-6.66	-5.26	-3.73		O	-8.32	-6.61	-5.20	-3.72
	Mg	-8.61	-7.02	-5.61	-4.18		Mg	-8.65	-6.94	-5.61	-4.19
	Si	-8.59	-7.02	-5.62	-4.20		Si	-8.59	-6.90	-5.59	-4.20
	Ca	-9.90	-8.30	-6.88	-5.41		Ca	-9.94	-8.25	-6.90	-5.42
	Fe	-8.82	-7.20	-5.76	-4.30		Fe	-8.86	-7.16	-5.77	-4.31
11000 K	He	-19.49	-14.30	-12.17	> -6.11	11500 K	He	-10.08	-6.51	-4.71	> -2.70
	O	-8.45	-6.77	-5.28	-3.73		O	-8.07	-6.44	-5.11	-3.73
	Mg	-8.76	-7.10	-5.65	-4.19		Mg	-8.41	-6.81	-5.55	-4.18
	Si	-8.66	-7.03	-5.62	-4.20		Si	-8.37	-6.82	-5.57	-4.20
	Ca	-10.05	-8.38	-6.90	-5.41		Ca	-9.66	-8.06	-6.81	-5.43
	Fe	-8.96	-7.29	-5.79	-4.30		Fe	-8.58	-6.99	-5.70	-4.32
11500 K	He	-19.51	-14.52	-12.42	> -7.70	12000 K	He	-9.73	-6.34	-4.64	> -3.60
	O	-8.47	-6.85	-5.39	-3.93		O	-7.92	-6.33	-5.00	-3.64
	Mg	-8.77	-7.18	-5.72	-4.35		Mg	-8.25	-6.72	-5.47	-4.12
	Si	-8.64	-7.11	-5.66	-4.35		Si	-8.22	-6.74	-5.49	-4.15
	Ca	-10.06	-8.50	-7.08	-5.54		Ca	-9.49	-7.94	-6.70	-5.33
	Fe	-8.97	-7.40	-5.94	-4.43		Fe	-8.42	-6.87	-5.59	-4.23
12000 K	He	-19.30	-13.16	-11.33	> -9.18	16000 K	He	-10.57	-6.09	-4.61	> -3.74
	O	-9.44	-6.40	-5.01	-4.86		O	-9.47	-6.44	-5.18	-4.75
	Mg	-9.14	-6.83	-5.48	-4.32		Mg	-9.16	-6.86	-5.67	-4.54
	Si	-8.91	-6.85	-5.50	-4.21		Si	-8.77	-6.88	-5.69	-4.44
	Ca	-11.06	-8.05	-6.70	-6.34		Ca	-11.09	-8.08	-6.90	-6.34
	Fe	-9.91	-6.97	-5.60	-4.89		Fe	-9.93	-6.98	-5.79	-5.01
16000 K	He	-18.27	-12.62	-10.52	> -7.88	20000 K	He	-8.73	-5.91	> -4.62	> -4.04
	O	-9.47	-6.56	-5.20	-3.81		O	-8.11	-6.55	-5.36	-4.92
	Mg	-9.17	-7.00	-5.67	-4.29		Mg	-8.39	-7.02	-5.86	-4.67
	Si	-8.77	-7.02	-5.69	-4.32		Si	-8.42	-7.04	-5.88	-4.57
	Ca	-11.09	-8.22	-6.89	-5.50		Ca	-9.66	-8.21	-7.07	-6.51
	Fe	-9.93	-7.13	-5.79	-4.40		Fe	-8.62	-7.11	-5.97	-5.15
20000 K	He	-16.40	-12.29	> -9.96	> -7.17	25000 K	He	-8.40	-5.80	> -4.70	> -3.91
	O	-8.13	-6.70	-5.36	-3.96		O	-8.22	-6.68	-5.55	-4.23
	Mg	-8.47	-7.14	-5.83	-4.45		Mg	-8.47	-7.22	-6.07	-4.72
	Si	-8.50	-7.16	-5.85	-4.48		Si	-8.51	-7.24	-6.09	-4.75
	Ca	-9.72	-8.36	-7.05	-5.66		Ca	-9.76	-8.38	-7.28	-5.93
	Fe	-8.66	-7.26	-5.95	-4.56		Fe	-8.70	-7.28	-6.18	-4.82
25000 K	He	-16.15	-12.20	> -9.46	> -6.59						
	O	-8.26	-6.83	-5.53	-4.14						
	Mg	-8.57	-7.27	-6.01	-4.62						
	Si	-8.61	-7.30	-6.03	-4.65						
	Ca	-9.84	-8.50	-7.23	-5.83						
	Fe	-8.76	-7.39	-6.13	-4.73						

We hope that our results, with the figures and tables, will be useful to provide realistic estimates of the accretion rates, including the effect of fingering convection, to be used for further studies on evolved planetary systems.

Table 6. Same as Table 3 for models with $M_{\text{H}} = 10^{-10} M_{\odot}$

	10^6 g s^{-1}	10^8 g s^{-1}	10^{10} g s^{-1}
10000 K	He	-7.59	-6.35
	O	-8.31	-6.47
	Mg	-8.60	-6.68
	Si	-8.55	-6.71
	Ca	-9.88	-8.03
	Fe	-8.80	-6.94
10500 K	He	-8.31	-6.30
	O	-8.28	-6.48
	Mg	-8.58	-6.70
	Si	-8.50	-6.66
	Ca	-9.86	-8.05
	Fe	-8.78	-6.96
11000 K	He	-8.76	-6.54
	O	-8.55	-6.80
	Mg	-8.86	-7.02
	Si	-8.70	-6.88
	Ca	-10.16	-8.37
	Fe	-9.07	-7.28
11500 K	He	-8.21	-5.98
	O	-8.03	-6.24
	Mg	-8.34	-6.48
	Si	-8.24	-6.48
	Ca	-9.59	-7.75
	Fe	-8.51	-6.71
12000 K	He	-9.68	-6.96
	O	-9.76	-7.87
	Mg	-9.21	-7.17
	Si	-9.16	-7.17
	Ca	-10.95	-8.98
	Fe	-9.75	-7.82
16000 K	He	-9.55	-7.04
	O	-9.73	-7.59
	Mg	-9.40	-7.22
	Si	-9.16	-7.04
	Ca	-11.33	-9.15
	Fe	-10.19	-8.02
20000 K	He	-9.56	-6.93
	O	-9.75	-7.60
	Mg	-9.40	-7.22
	Si	-9.12	-6.99
	Ca	-11.34	-9.16
	Fe	-10.20	-8.03
25000 K	He	-9.35	-5.68
	O	-9.76	-5.94
	Mg	-9.41	-6.14
	Si	-9.03	-6.22
	Ca	-11.35	-7.44
	Fe	-10.20	-6.46

Acknowledgements. This work was supported by PICT-2017-0884 from AN-PCyT, PIP 112-200801-00940 grant from CONICET, and grant G149 from University of La Plata. This research has made use of NASA Astrophysics Data System. F.C.W., G.V. and S.V. acknowledge financial support from "Programme National de Physique Stellaire (PNPS)" of CNRS/INSU, France.

References

Alexander, D. R. & Ferguson, J. W. 1994, *ApJ*, 437, 879
Allègre, C., Manhès, G., & Lewin, É. 2001, *Earth and Planetary Science Letters*, 185, 49

Althaus, L. G., Camisassa, M. E., Miller Bertolami, M. M., Córscico, A. H., & García-Berro, E. 2015, *A&A*, 576, A9
Althaus, L. G., Serenelli, A. M., Córscico, A. H., & Montgomery, M. H. 2003, *A&A*, 404, 593
Althaus, L. G., Serenelli, A. M., Panei, J. A., et al. 2005, *A&A*, 435, 631
Bauer, E. B. & Bildsten, L. 2018, *ApJ*, 859, L19
Bauer, E. B. & Bildsten, L. 2019, *ApJ*, 872, 96
Brown, J. M., Garaud, P., & Stellmach, S. 2013, *ApJ*, 768, 34
Burgers, J. M. 1969, *Flow Equations for Composite Gases*
Christensen-Dalsgaard, J., Silva Aguirre, V., Cassisi, S., et al. 2020, *A&A*, 635, A165
Cunningham, T., Tremblay, P.-E., Bauer, E. B., et al. 2021, *MNRAS*, 503, 1646
Cunningham, T., Tremblay, P.-E., Freytag, B., Ludwig, H.-G., & Koester, D. 2019, *MNRAS*, 488, 2503
Deal, M., Deheuvels, S., Vauclair, G., Vauclair, S., & Wachlin, F. C. 2013, *A&A*, 557, L12
Debes, J. H. & López-Morales, M. 2008, *ApJ*, 677, L43
Debes, J. H. & Sigurdsson, S. 2002, *ApJ*, 572, 556
Debes, J. H., Walsh, K. J., & Stark, C. 2012, *ApJ*, 747, 148
Farihi, J., Gänsicke, B. T., & Koester, D. 2013, *Science*, 342, 218
Farihi, J., Gänsicke, B. T., Wyatt, M. C., et al. 2012, *MNRAS*, 424, 464
Frewen, S. F. N. & Hansen, B. M. S. 2014, *MNRAS*, 439, 2442
Gänsicke, B. T., Aungwerojwit, A., Marsh, T. R., et al. 2016, *ApJ*, 818, L7
Gänsicke, B. T., Koester, D., Farihi, J., et al. 2012, *MNRAS*, 424, 333
Garaud, P. 2011, *ApJ*, 728, L30
Gary, B. L., Rappaport, S., Kaye, T. G., Alonso, R., & Hamschs, F. J. 2017, *MNRAS*, 465, 3267
Grossman, S. A., Narayan, R., & Arnett, D. 1993, *ApJ*, 407, 284
Hoskin, M. J., Toloza, O., Gänsicke, B. T., et al. 2020, *MNRAS*, 499, 171
Iglesias, C. A. & Rogers, F. J. 1996, *ApJ*, 464, 943
Izquierdo, P., Rodríguez-Gil, P., Gänsicke, B. T., et al. 2018, *MNRAS*, 481, 703
Jura, M. 2003, *ApJ*, 584, L91
Koester, D. 2009, *A&A*, 498, 517
Koester, D., Gänsicke, B. T., & Farihi, J. 2014, *A&A*, 566, A34
Koester, D. & Wilken, D. 2006, *A&A*, 453, 1051
Manser, C. J., Gänsicke, B. T., Eggl, S., et al. 2019, *Science*, 364, 66
Melis, C. & Dufour, P. 2017, *ApJ*, 834, 1
Miller Bertolami, M. M. 2016, *A&A*, 588, A25
Mustill, A. J., Villaver, E., Veras, D., Bonsor, A., & Wyatt, M. C. 2013, in *European Physical Journal Web of Conferences*, Vol. 47, *European Physical Journal Web of Conferences*, 06008
Raddi, R., Gänsicke, B. T., Koester, D., et al. 2015, *MNRAS*, 450, 2083
Rappaport, S., Gary, B. L., Kaye, T., et al. 2016, *MNRAS*, 458, 3904
Reach, W. T., Lisse, C., von Hippel, T., & Mullally, F. 2009, *ApJ*, 693, 697
Redfield, S., Farihi, J., Cauley, P. W., et al. 2017, *ApJ*, 839, 42
Renedo, I., Althaus, L. G., Miller Bertolami, M. M., et al. 2010, *ApJ*, 717, 183
Salaris, M., Althaus, L. G., & García-Berro, E. 2013, *A&A*, 555, A96
Silva Aguirre, V., Christensen-Dalsgaard, J., Cassisi, S., et al. 2020, *A&A*, 635, A164
Stancliffe, R. J., Glebbeek, E., Izzard, R. G., & Pols, O. R. 2007, *A&A*, 464, L57
Swan, A., Farihi, J., Koester, D., et al. 2019, *MNRAS*, 490, 202
Vanderburg, A., Johnson, J. A., Rappaport, S., et al. 2015, *Nature*, 526, 546
Vauclair, S. 2004, *ApJ*, 605, 874
Veras, D. 2016, *Royal Society Open Science*, 3, 150571
Veras, D., Eggl, S., & Gänsicke, B. T. 2015a, *MNRAS*, 452, 1945
Veras, D., Eggl, S., & Gänsicke, B. T. 2015b, *MNRAS*, 451, 2814
Veras, D., Jacobson, S. A., & Gänsicke, B. T. 2014a, *MNRAS*, 445, 2794
Veras, D., Leinhardt, Z. M., Bonsor, A., & Gänsicke, B. T. 2014b, *MNRAS*, 445, 2244
Veras, D., Leinhardt, Z. M., Eggl, S., & Gänsicke, B. T. 2015c, *MNRAS*, 451, 3453
Veras, D., Mustill, A. J., Bonsor, A., & Wyatt, M. C. 2013, *MNRAS*, 431, 1686
Veras, D., Mustill, A. J., Gänsicke, B. T., et al. 2016, *MNRAS*, 458, 3942
Wachlin, F. C., Miller Bertolami, M. M., & Althaus, L. G. 2011, *A&A*, 533, A139
Wachlin, F. C., Vauclair, G., Vauclair, S., & Althaus, L. G. 2017, *A&A*, 601, A13
Wachlin, F. C., Vauclair, S., & Althaus, L. G. 2014, *A&A*, 570, A58
Wilson, D. J., Gänsicke, B. T., Koester, D., et al. 2019, *MNRAS*, 483, 2941
Wilson, D. J., Gänsicke, B. T., Koester, D., et al. 2015, *MNRAS*, 451, 3237
Xu, S., Zuckerman, B., Dufour, P., et al. 2017, *ApJ*, 836, L7
Zemskova, V., Garaud, P., Deal, M., & Vauclair, S. 2014, *ApJ*, 795, 118
Zuckerman, B. & Becklin, E. E. 1987, *Nature*, 330, 138

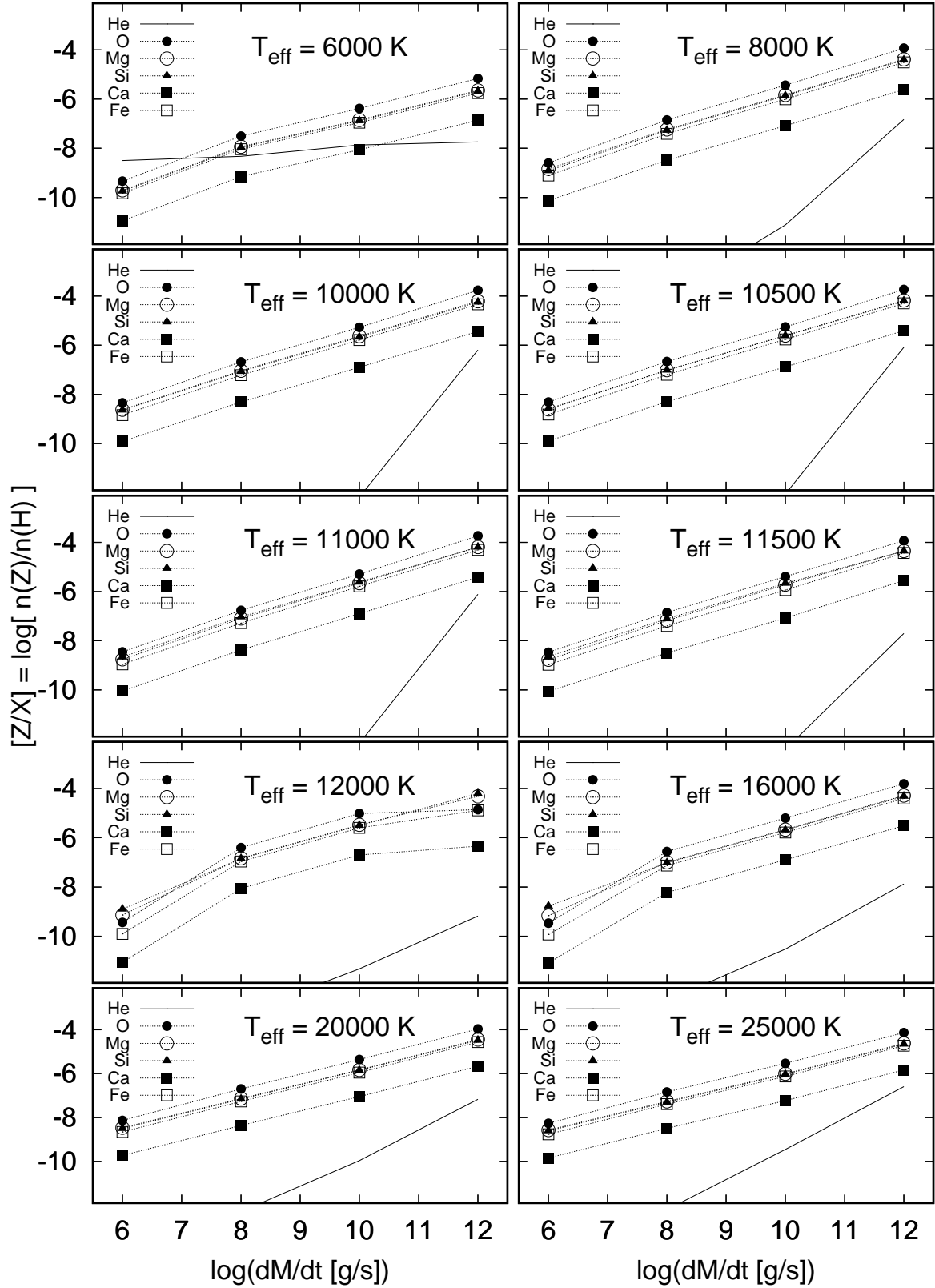


Fig. 10. Same as Figure 9 for models with $M_H = 10^{-6} M_\odot$.

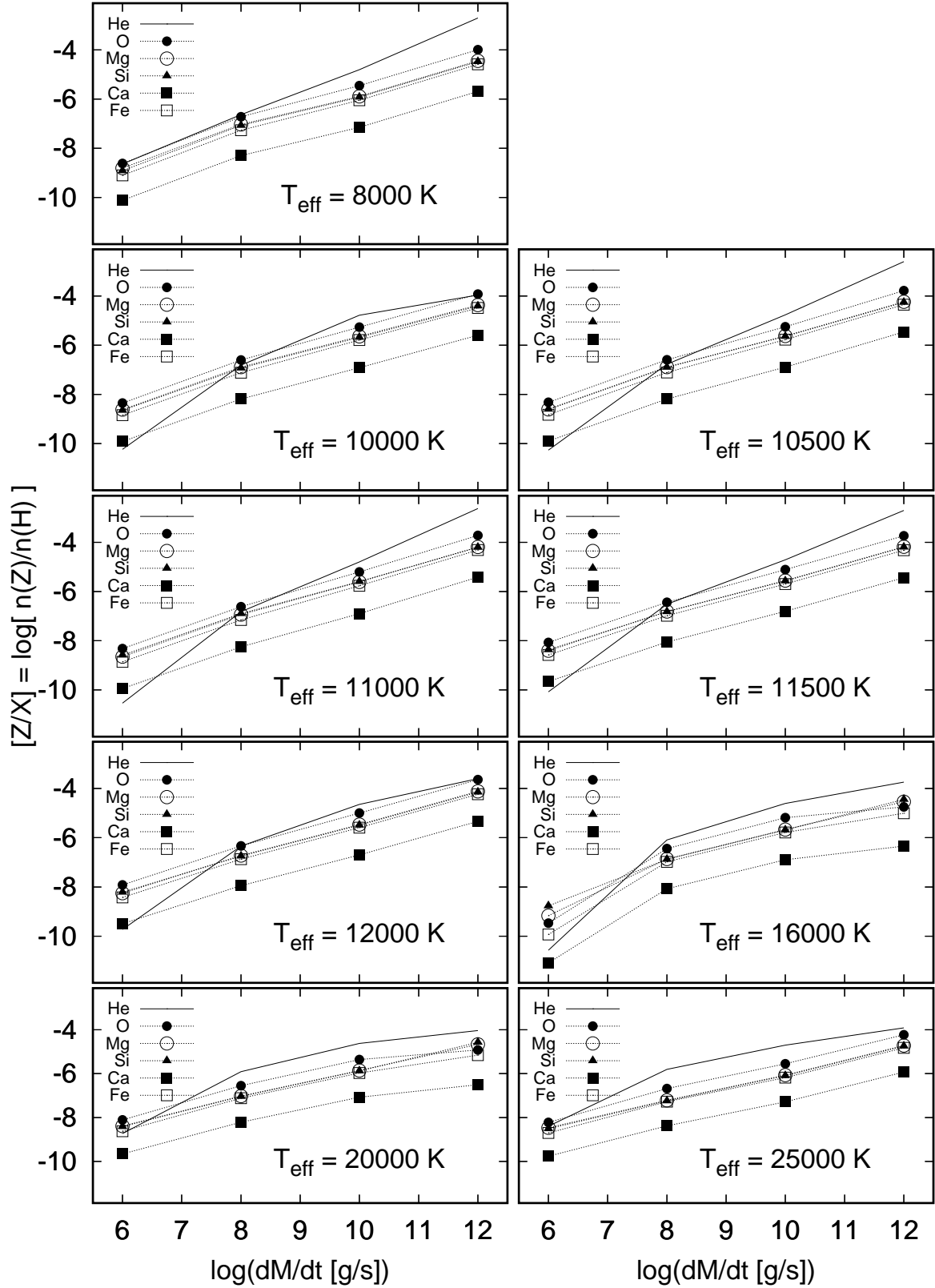


Fig. 11. Same as Figure 9 for models with $M_{\text{H}} = 10^{-8} M_{\odot}$.

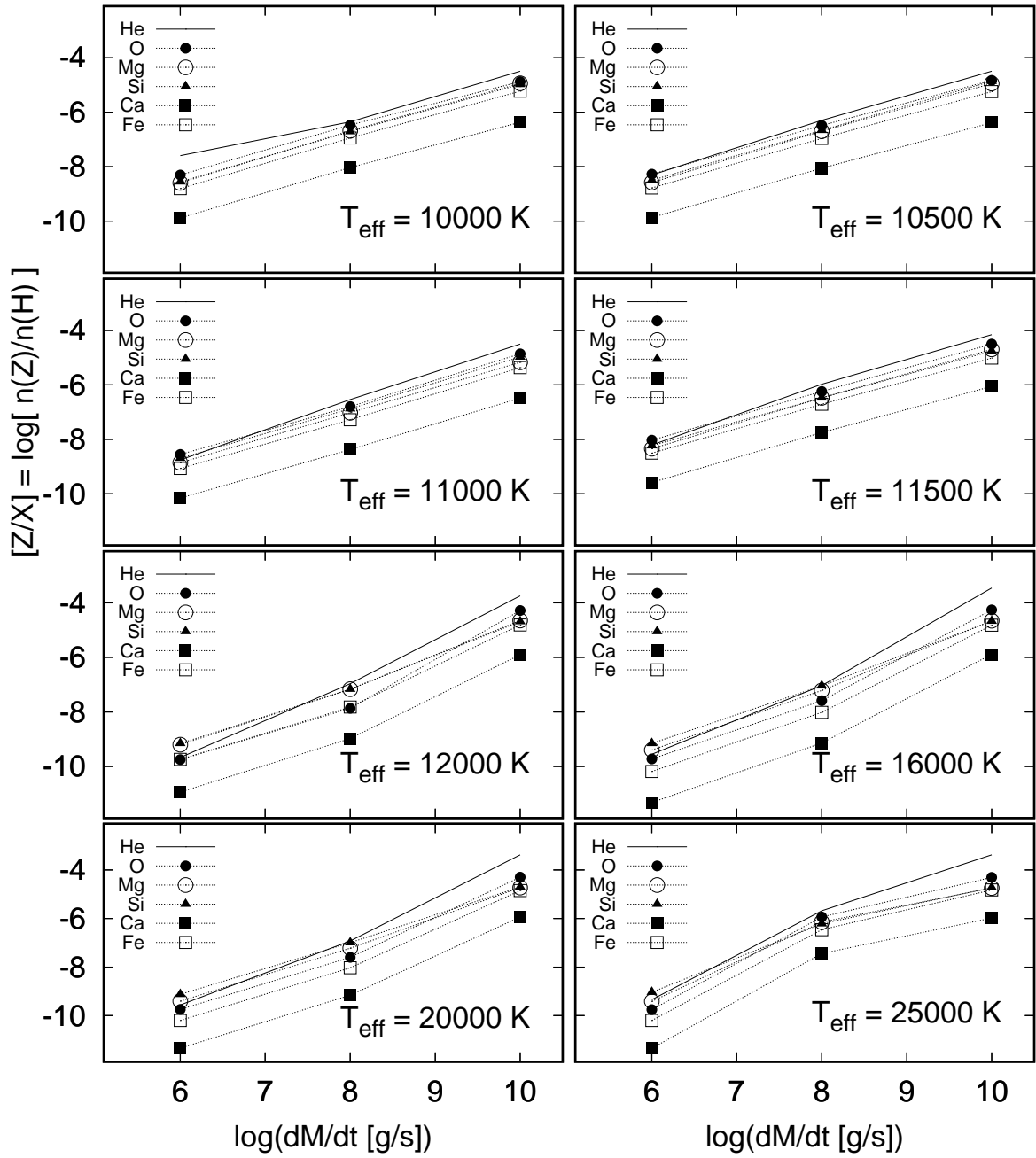


Fig. 12. Same as Figure 9 for models with $M_{\text{H}} = 10^{-10} M_{\odot}$.